Understanding Sampling Bias in the Global Heat Flow Compilation

Tobias Stål [1,2,3*], Anya M. Reading [1,2,3], Sven Fuchs [4], Jacqueline A. Halpin [2,3], Mareen Lösing [5], Ross J. Turner [1]

[1] *School of Natural Sciences (Physics), University of Tasmania, Hobart, Tasmania 7001, Australia*
[2] *Institute for Marine and Antarctic Studies, University of Tasmania, Hobart, Tasmania 7004, Australia*
[3] *The Australian Centre for Excellence in Antarctic Science (ACEAS), University of Tasmania, Hobart, Tasmania 7001, Australia*
[4] *Section Geoenergy, Helmholtz Centre Potsdam - GFZ German Research Centre for Geosciences, Potsdam, Germany*
[5] *Institute of Geosciences, Kiel University, Kiel, Germany*

Correspondence*:
Tobias Stål
tobias.staal@utas.edu.au

ABSTRACT

Geothermal heat flow is commonly inferred from the gradient of temperature values in boreholes. Such measurements are expensive and logistically challenging in remote locations and, therefore, often targeted to regions of economic interest. As a result, measurements are not distributed evenly. Some tectonic, geologic and even topographic settings are overrepresented in global heat flow compilations; other settings are underrepresented or completely missing. These limitations in representation have implications for empirical heat flow models that use catalogue data to assign heat flow by the similarity of observables.

In this contribution, we analyse the sampling bias in the Global Heat Flow Database of the International Heat Flow Commission (IHFC), the most recent and extensive heat flow catalogue, and discuss the implications for accurate prediction and global appraisals. We also suggest correction weights to reduce the bias when the catalogue is used for empirical modelling.

From comparison with auxiliary variables, we find that each of the following settings is highly overrepresented for heat flow measurements; continental crust, sedimentary rocks, volcanic rocks, and Phanerozoic regions with hydrocarbon exploration. Oceanic crust, cratons, and metamorphic rocks are underrepresented. The findings also suggest a general tendency to measure heat flow in areas where the values are elevated; however, this conclusion depends on which auxiliary variable is under consideration to determine the settings. We anticipate that the use of our correction weights to balance disproportional representation will improve empirical heat flow models for remote regions and assist in the ongoing assessment of the Global Heat Flow Database.

Keywords: heat flow, geothermal, sampling bias, compilation, thermal, regionalisation, geomorphometrics

1 INTRODUCTION

Studies of geothermal heat provide essential insight into the internal structure and history of the Earth (Kelvin, 1863; Beardsmore and Cull, 2001). A range of mechanisms control the amount of heat observed: thermal properties of the upper mantle, ongoing or recent tectonism (e.g. Pasquale et al., 2014; Goes et al., 2020), crustal heat production (e.g. Jaupart et al., 2016; Hasterok et al., 2018), topographic focusing by refraction (e.g. Lees et al., 1910), erosion and sedimentation (e.g. Von Herzen and Uyeda, 1963), advection by groundwater (e.g. Mansure and Reiter, 1979), and preserved variations and anomalies of paleoclimatic conditions (e.g. Huang et al., 1997; Šafanda et al., 2004).

Insights from geothermal measurements are applied in mineral prospecting (e.g. Cull et al., 1988), and hydrocarbon exploration, for example, to constrain the oil and gas windows (e.g. Royden and Sclater, 1980; Shalaby et al., 2011), and geothermal energy (Dickson and Fanelli, 2013). One particular aspect of geothermal heat flow that has recently gained attention is the impact of heat transfer at the base of ice sheets in Greenland and Antarctica (Burton-Johnson et al., 2020; Karlsson et al., 2021; Colgan et al., 2022). Even moderate geothermal heat can generate basal melting at the pressure melting point, reducing the friction of ice over bedrock or sediment and changing the rheology of the ice (Greve and Hutter, 1995; Pattyn, 2010).

Heat flow is calculated from the thermal gradient in a borehole combined with measurements or assumptions regarding thermal conductivity. Factors that impact the uncertainty and reproducibility of the recorded heat flow include the depth of the borehole, integration time for bore fluid to equilibrate to the surrounding temperature, assumptions regarding thermal conductivity, and groundwater flow (Beardsmore and Cull, 2001). Most measurements have been conducted in the northern hemisphere, particularly in Western North America and Southern Europe (Fig. 1A). Measurements are costly and often sparse in remote areas (Fig. 1C-D). A few techniques have been established to generate continuous maps where in-situ measurements are unavailable. Forward models compute heat flow values from thermal gradients modelled from geophysical data (An et al., 2015; Martos et al., 2017; Gard and Hasterok, 2021), energy balance (Stål et al., 2020a), geological association (Davies and Davies, 2010; Burton-Johnson et al., 2017), or isostasy (Hasterok and Gard, 2016). Each of these approaches is associated with assumptions, particularly regarding to the crustal heat production and the strength of association between the dataset used and observed heat flow (Ebbing et al., 2009; Haeger et al., 2019; Lösing et al., 2020). A different approach has been to interpolate and model heat flow empirically by linking heat flow measurements elsewhere to a target through the similarity of one or many observables (Goutorbe et al., 2011; Lucazeau, 2019; Shen et al., 2020; Stål et al., 2020b; Li et al., 2021; Lösing and Ebbing, 2021). This empirical approach shows promising and converging results in the case of Antarctica; however, the choice of observables and how well they capture thermal properties have been discussed and challenged (Davies and Davies, 2010; Stål et al., 2020b; Artemieva, 2022), and further analysis will likely refine the choices made.

One aspect of empirical heat flow studies that has attracted less debate, but has the potential to impact the results, is the representation of the reference heat flow catalogue. Stål et al. (2020b) suggest that a focus on economic exploration, particularly, in the Gondwana continents (e.g. Africa and Australia), could lead to sampling bias. Another potential factor that might skew the representation of the catalogue is a tendency to drill in flat and accessible locations within mountainous regions. Heat flow values are sometimes corrected for topographic factors, but not always, and it can be difficult to determine if such corrections have been applied in older studies. Such clarifications are within the scope of the ongoing Global Heat Flow Data Assessment Project of the IHFC catalogue (Fuchs et al., 2021a).

In this contribution, we analyse the most recent and extensive heat flow catalogue (Fuchs et al., 2021b) for factors that might bias the distribution and hence impact the integrated heat flow maps. We also discuss qualitative reasons for the uneven distribution and suggest statistical weights of individual samples for use when the catalogue finds ongoing use.

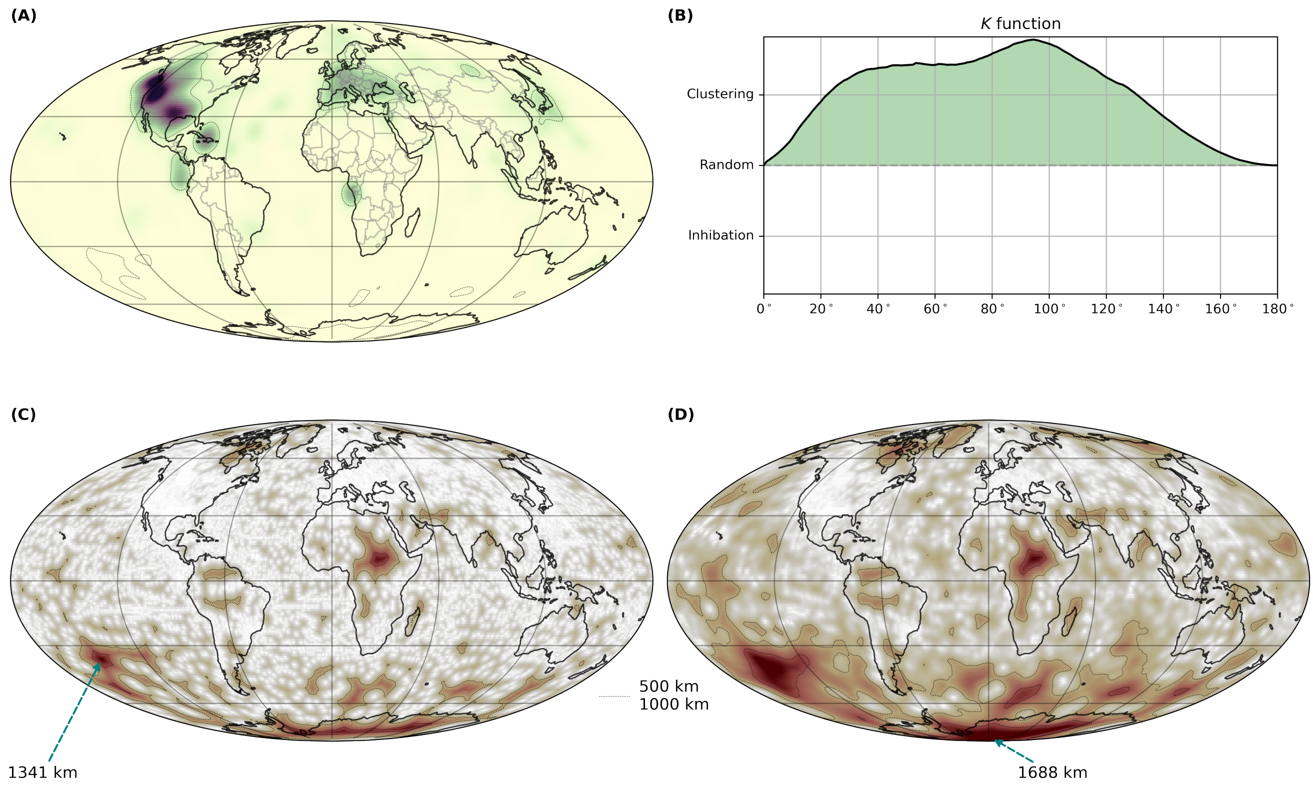

Figure 1. Geographic distribution of heat flow measurements. **(A)** Kernel density estimation (KDE) for density of heat flow measurements, using great circle distances and a Gaussian kernel with σ = 400 km. The threshold is set to the 5% percentile. **(B)** Centred Ripley's K function plot, where the positive values indicate that measurements are heavily clustered on all scales, with a peak at $90°$. **(C)** Distance to the nearest measurement. The longest distance is 1341 km, at 37°S 148°W in the South Pacific Ocean. **(D)** Mean distance to nearest ten measurements. The longest distance is 1688 km, at 85°S 8°E in East Antarctica. Contours indicate 500 km and 1000 km distances in **(C)** and **(D)**. Maps are displayed with perceptually linear colour representation (Crameri and Shephard, 2019; Morse et al., 2019) using *matplotlib* (Hunter, 2007).

2 METHOD

Spatial characteristics of the data are analysed to quantify clustering and misrepresentation. The analysis is carried out using Python libraries: *geopandas* (Jordahl, 2014), *rasterio* (Gillies, 2019), and *numpy* (Harris et al., 2020). Methods are implemented from *agrid* (Stål and Reading, 2020), a python-based grid for representing multidimensional geophysical data. All code is made available to ensure reproducibility, and all datasets used are provided in open repositories.

2.1 Heat flow database

We include the entire IHFC catalogue (cf. Fuchs et al. (2021b)), except for 12 records where positional data is missing. All remaining 74 536 entries are analysed as they appear. We treat every given location as correct and precise; however, this is often not the case for older records.

2.2 Spatial descriptive statistics

We use a kernel density estimate (KDE) function to first appraise the spatial distribution of the heat flow measurements (Fig. 1A). The KDE is calculated from a Gaussian kernel (σ = 400 km) applied to the spatial distribution of heat flow measurements. We also calculate the distance in kilometres to the nearest measurement and the mean distance to the nearest ten measurements on a $1^\circ \times 1^\circ$ grid (Fig. 1C-D). All distance calculations are done using the haversine formula, assuming a spherical Earth.

For an appraisal of clustering, we calculate Ripley's centred K functions (Dixon, 2014) (Fig. 1B). The standard application is modified for great circle distances (Stål, 2022). The distribution of pair-wise distances is also presented as a histogram in Figure S2.

2.3 Area weighting

We compute a geometric area weighting, assigning a higher weight to sparse records, and a lower weight to densely located measurements. This approach does not take the geological setting into account. For each record, we first weigh other records by proximity from a Gaussian kernel so that the impact decreases with the distance. We apply three different Gaussian kernels with $\sigma = 50$ km, 200 km, and 1000 km. The weight for each record in IHFC is calculated from the inverse proximity weight divided by the mean inverse proximity weight for all records (Fig. S5).

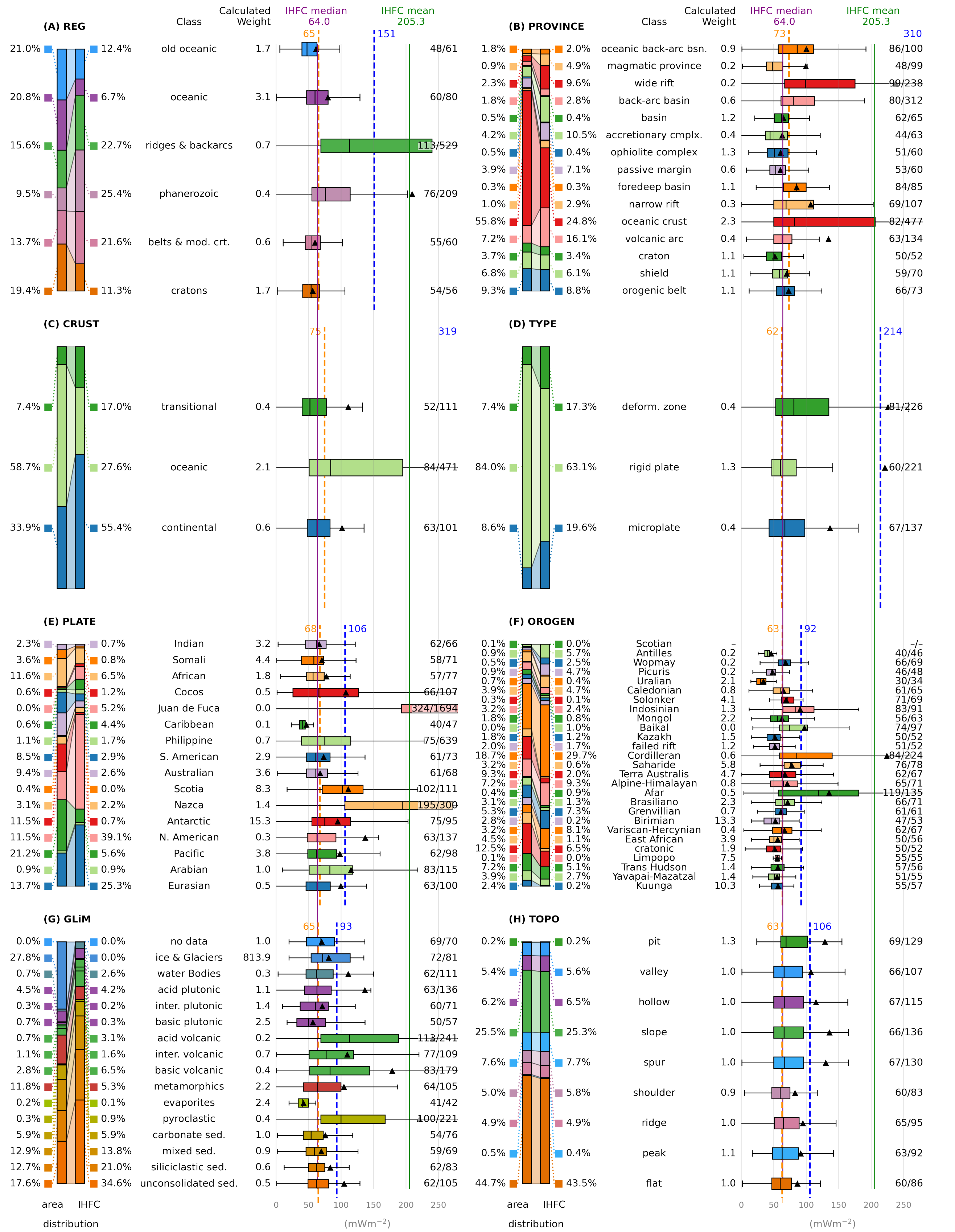

Figure 2. (Caption next page.)

Figure 2. (Previous page.) Categorical classes in auxiliary variables, as sampled and heat distribution for each class. **(A)** Regionalisation from seismic surface wave tomography (Schaeffer and Lebedev, 2015) **(B)** Province type (Hasterok et al., 2022) **(C)** Crustal type (Hasterok et al., 2022) **(D)** Tectonic plate type (Hasterok et al., 2022) **(E)** Tectonic plate name (Hasterok et al., 2022) **(F)** Last orogeny (Hasterok et al., 2022) **(G)** Lithological class (Hartmann and Moosdorf, 2012) **(H)** Geomorphometric shape (Amatulli et al., 2020) From left to right within each subplot: Percentage of the relative distribution of the class of auxiliary variable calculated for an equal-area projection, shown numerically and as a bar plot (left bar). Percentage of the relative distribution of the class of the location measurement in IHFC are shown as a bar plot (right bar) and numerically. The calculated weight for each class to compensate for the difference between the distributions. The horizontal box plots show the heat flow distribution for measurements within each class. The mean heat flow for each class is indicated by a black triangular marker (▲). The median heat flow for each class is indicated with the vertical line (|) within each box. Note that a few whiskers and bars are cropped. Outliers are not indicated. Each class median and mean value is also given numerically in the rightmost column. Weighted average heat flow for each auxiliary variable shown as a dashed blue vertical line and given numerically in blue at the top. The value is calculated by assigning the mean heat flow for each class to the reference area. The median values for the weighted means are shown as a dashed orange vertical line and a numerical value in orange at the top. The vertical lines indicate the mean (green; 205.3 mWm^{-3}) and median (purple; 64 mWm^{-3}) values of all IHFC database records (Fuchs et al., 2021b). Abbreviation used in the labels; bsn. = basin, cmplx = complex, interm. = intermediate, belts & mod. crt. = Precambrian belts and modified cratons, sed. = sediments or sedimentary rocks. All heat flow values are given in $\mathrm{mW\,m^{-2}}$; units are omitted to minimise clutter.

2.4 Auxiliary variables from categorical maps

We examine the sampling bias in heat flow measurements for eight categorical auxiliary variables, which do not directly correlate with observed geothermal heat flow but can be used to investigate the spatial distribution. The selection of those variables is based on three criteria:

1. Has global or near-global extent with consistent quality and uniform resolution; however, datasets excluding oceanic settings are considered. Particularly, the observables should be comparable for Gondwanan continents and the rest of the world.
2. Represents parameters with expected auxiliary impact on the heat flow distribution.
3. Is available with open access to a computer-readable format.

Auxiliary variable values at each heat flow location are sampled using spatial join for vector polygon datasets or point sampling to the nearest pixel for data sets provided as rasters. Those values are added as attribute data to the database file analysed (this modified database is provided in supplementary material). The relative reference area distribution of each class is calculated from the dataset used, excluding undefined area. Vector polygon areas are calculated in an equal-area projection, and global rasters are compensated with a function that weights each pixel to the area it represents on a sphere. All tectonic, geological or geomorphometric classes for each auxiliary variable are listed in Figure 2. We also calculate the relative distribution of two cultural datasets to investigate the reasons for the sampling bias (Fig. 3).

2.4.1 Tectonic variables

We include the regionalisation from clustering of surface wave tomography (Schaeffer and Lebedev, 2015) (labelled as REG), which provides a quantitative, robust global regionalisation (Fig. 2A). We also include the recent tectonic and geologic province maps (Hasterok et al., 2022), these maps are constructed from refined qualitative and quantitative analyses of published global and regional maps, and auxiliary geoscientific data sets such as earthquake locations and geochronology. We analyse for the following:

Province type (PROVINCE), for example, craton, passive margin, basin (Fig. 2B); Crust type (CRUST), i.e. continental, oceanic, transitional crust (Fig. 2C); Plate type (TYPE), i.e. microplate, rigid plate, deformation zone (Fig. 2D). Tectonic plate (PLATE), for example, Philippine Plate, Antarctic Plate, and Somali Plate (Fig. 2E). We also investigate the most recent orogeny (OROGEN), for example, Alpine-Himalayan, Grenvillian, and Afar (Fig. 2F). This dataset provides a first-order approximation of crustal stabilisation age.

2.4.2 Geological variables

Lithological affiliation is sampled from the GLiM map (Hartmann and Moosdorf, 2012). The map is assembled from existing regional geological maps translated into 16 classes (for example, unconsolidated sediments, metamorphics, and basic volcanic rocks). The relative abundance of each class only considers the land area as the geology of oceanic regions is not provided; however, we include classes such as water bodies, and ice and glaciers (Fig. 2G).

2.4.3 Geomorphometric variables

Topographic refraction is a well-known parameter to locally focus heat (Lees et al., 1910). A recent set of geomorphometrics rasters (Amatulli et al., 2020) provides insights into the shape of the topography from a high-resolution global digital elevation model (Yamazaki et al., 2017). One raster with particular relevance for a first appraisal is the geomorphological forms (Jasiewicz and Stepinski, 2013; Amatulli et al., 2018). The shape is associated with ten classes such as ridge, summit, and slope (TOPO, Fig. 2H). For efficient area distribution calculation, we sub-sample the raster at a ratio of 1:40 (Fig. S1). Point sampling at heat flow measurements is done in full resolution, 250 m at the equator, corresponding to 0.00208 degrees.

2.4.4 Cultural variables

We investigate the economic setting for where heat flow measurements have been conducted. Prospecting and exploration are linked to geology as well as infrastructure and accessibility. We count the fraction of heat flow measurements within oil and gas fields (Rose et al., 2018). We also count the number of measurements within 0.5 degrees distance from mining sites, derived from reported activities and infrastructure identified from satellite images (Maus et al., 2020). Cultural auxiliary variable polygons are dissolved to remove any overlapping polygons.

As a reference for both cultural datasets, we use the total area of the Earth's landmass 148 940 000 km^2; however, data points in offshore oil and gas fields are included, and hence the total reference area is slightly larger than 100%. (Fig. 3A-B). We also investigate the Australian case for an appraisal of the impact in a region known for mining and hydrocarbon exploration and relevant for an understanding of East Antarctic geothermal heat distribution. The reference Australian landmass area is 7 692 024 km^2 (Fig. 3B-C).

2.5 Calculation of weights

For each auxiliary variable, a weight is calculated for sample balancing as the quotient ratio of the fraction of reference area covered by a given class, and the fraction of heat flow measurements taken from the matching setting:

$$w(c) = \frac{f_A(c)}{f_N(c)}, \tag{1}$$

where $w(\mathrm{c})$ is the calculated weight for each class or category (c), $f_A(c)$ is the area fraction of the reference area; entire globe, terrestrial landmass (TOPO and GliM), or all orogens (OROGEN), and $f_N(c)$ is the

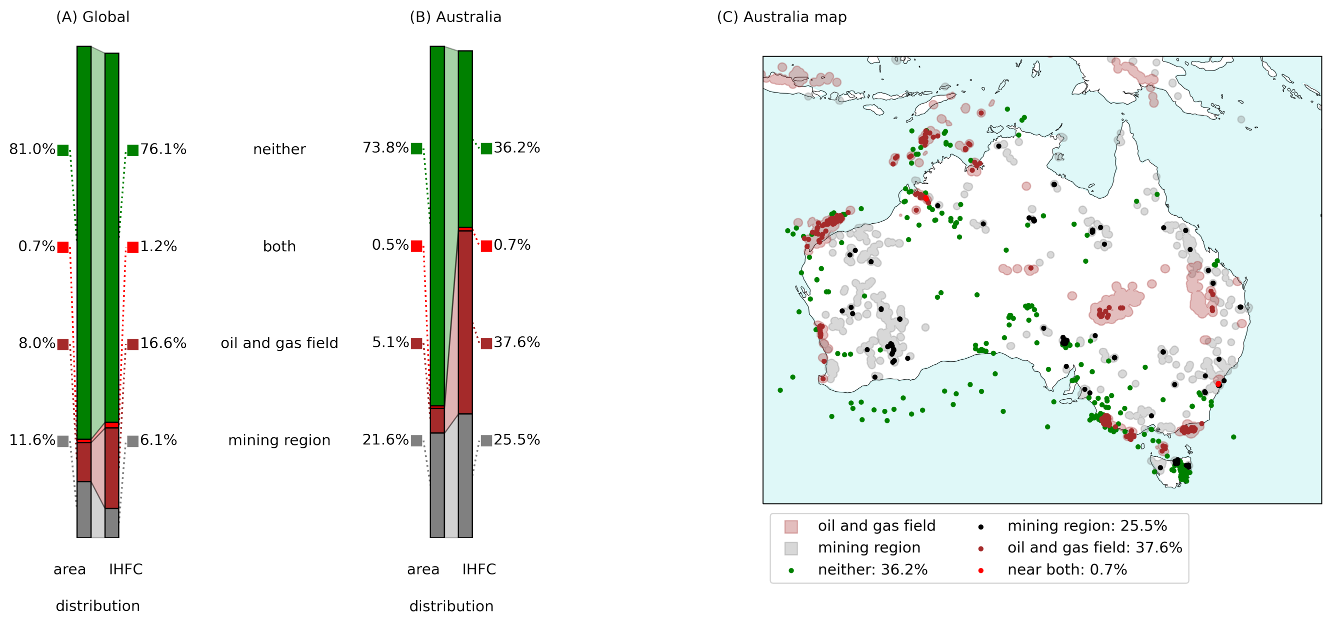

Figure 3. Correlation with mining and hydrocarbon prospecting and exploration. **(A)** The area distribution for mining polygons (grey), oil and gas fields (brown), overlapping mining region and oil field (red), and neither mining nor oil and gas fields near the measurement (green, as explained in Fig. 2). The reference land area is the global landmass; however, offshore oil and gas fields are included, making the total slightly over 100%. **(B)** The same distribution for Australia. The area distribution of Australian oil fields (392.591 km^2)(Rose et al., 2018) and mining regions (Maus et al., 2020) with a buffer, as described in the text (1.657.683 km2). The reference area is the Australian landmass (7.692.024 km2). **(C)** Map of Australia showing mine sites (Maus et al., 2020) with a buffer of 0.5° and gas fields (Rose et al., 2018).

fraction of measurements in IHFC located within the area of the class. The weights for each auxiliary variable are assigned to each record for the class it is located within. Weights for four auxiliary variables are shown in Fig. 4A-D, and for all variables in Fig. S3.

Some auxiliary variables are correlated because they represent comparable properties in their respective studies or by the nature of geological processes (Fig. S5). Combining weights is not straightforward, and various techniques with different benefits and shortcomings produce diverging results (Reviewed by Kalton, G. and Flores-Cervantes, 2003). A well-established approach is iterative proportional fitting (IPF), sometimes referred to as *raking*. IPF is an iteratively-calculated weight for each combination of classes between the N variables that satisfies the marginal distribution for each variable. We compute combined weights using the Python package *ipfn* (Forthommme, 2021). There is no theoretical upper limit to how many variables can be fitted; however, attempts to fit more than four variables return non-robust high weights, and the computational cost increases exponentially with the number of variables. Individual records can be assigned very high weight if underrepresented in more than one auxiliary variable.

We calculate joint weighting for all combinations of 2, 3 or 4 auxiliary variables, yielding a total of $\sum_{k=2,3,4} \binom{8}{k} = 154$ combinations. All fitted weights are added to the catalogue. Weighted mean, weighted median and difference from estimated global average is listed in Table S2, S3 and S3.

We assume that a reasonable indication of the soundness of a weighting is that the weighted average is closer to the estimated global average 80 $\mathrm{mW\,m^{-2}}$ (Lucazeau, 2019) than the mean of the catalogue, 205

$\mathrm{mW\,m^{-2}}$. As such, we rank the weightings by decreasing the difference from 80 $\mathrm{mW\,m^{-2}}$ (Lucazeau, 2019). This is not a universal validation but allows us to consider what properties are meaningful.

3 RESULTS

An overview of the spatial distribution of records is shown as a kernel density estimation in Figure 1A. This smoothed distribution highlights that the highest density of measurements is in the Western USA and Southern Europe. Figure 1B shows Ripley's K functions. For context, the expected value of the K function for spatially uniform sampling is $\widehat{K}(t) = 0$. The measured K function is positive on all scales, indicating clustering.

Figure 1C shows the distance to the nearest IHFC heat flow record, measured from grid cell centres. Central Africa, the Amazon Basin, and parts of the Middle East, have extensive areas with a distance of over 500 km to the nearest record. In parts of interior Africa there are areas with over 1000 km, and up to 1341 km in South Pacific. Figure 1D shows the mean distance to the closest ten measurements. The overall distribution is similar; however notably, the Southern Ocean is highlighted as having only a few measurements representing large areas. For both metrics, Antarctica is exceptionally sparsely surveyed.

In Figure 2, we show the reference and sampled distributions and the heat flow associated with each class for the eight categorical auxiliary variables. The calculated weights are listed. The horizontal bar charts show the heat distribution within each class, supplemented with calculated mean and median heat flow. Generally, the mean heat flow values tend to be much higher than the median due to extremely high measurements in active geothermal settings. The difference between the median and mean values of IHFC and the weighted average heat flow indicates the magnitude of the impact on heat flow models from sampling bias. We also calculate the robust mean, excluding 1 and 10% upper and lower percentiles (Supplementary material Table S1).

To better understand the origin of the sampling bias, we extract the economic setting for the measurements: 17.8% of the measurements in IHFC are within the polygons defined as oil and gas fields (Rose et al., 2018), in relation to only 8.7% of the landmass. Meanwhile, 7.3% of the measurements are within 0.5° from a mine, as mapped (Maus et al., 2020), in relation to 12.3% of the global landmass, excluding oceans. Prospective regions are only slightly over-represented on a global average; however strongly pronounced in sparsely populated Australia, where 26.2% of the measurements in IHFC are located in mining areas (c.f. 22.1% by landmass), as defined above, and 38.3% of the measurements are within oil and gas fields (c.f. 5.6% by landmass, Rose et al. (2018)). Moreover, many of the remaining measurements are in regions targeted for geothermal heat extraction, e.g. North West Tasmania and South-Western Victoria (Bahadori et al., 2013; Holgate et al., 2010). Figure 3C shows the Australian records in IHFC and the polygons used to define mining and oil and gas fields.

Figure 4 shows the weights calculated. Figure 4A shows the weights derived from seismic tomography regionalisation (Schaeffer and Lebedev, 2015), highlighting the general under-representation of the oceanic crust. Figure 4B shows the smaller weights from geomorphometrics (Amatulli et al., 2020). For this analysis, local rather than global distribution impacts the weight. Figure 4C shows the weights based on the province (Hasterok et al., 2022). Figure 4D shows the weights from lithologies (Hartmann and Moosdorf, 2012). Oceans are set to a weight of 1. All ten maps are provided in Supplementary material Figure S4.

We now consider selected weights derived for the classes in each auxiliary variable using IPF, as described in Section 2.5.

The IPF calculated weighting from TYPE and TOPO produce a weighted average of 84 $\mathrm{mW\,m^{-2}}$, this is closest to the estimated global mean (Lucazeau, 2019; Pollack et al., 1993), and also the lowest weighted mean for any fitted weighting. The weighted median is 58 $\mathrm{mW\,m^{-2}}$, which is lower than the median of IHFC, 64 $\mathrm{mW\,m^{-2}}$ (Fig. 4E). IPF calculated weighting from the three variables CRUST, TYPE, and PLATE yield a weighted mean of 93 $\mathrm{mW\,m^{-2}}$, which is also close to expected global average. The weighted median is 60 $\mathrm{mW\,m^{-2}}$ (Fig. 4F). An IPF calculated weighting from a combination with potential to capture both tectonic and geological misrepresentation, TYPE and GLiM, gives a weighted mean of 95 $\mathrm{mW\,m^{-2}}$, and a weighted median is 58 $\mathrm{mW\,m^{-2}}$ (Fig. 4G). An IPF calculated weighting from TYPE, GLiM, and TOPO represent tectonic, geological and topographic settings. The weighted mean for this combination is 145 $\mathrm{mW\,m^{-2}}$, and the weighted median is 59 $\mathrm{mW\,m^{-2}}$ (Fig. 4H)

From all variables considered, some extreme weights are suggested. In order to compensate for the sparse measurements from GliM class *glaciers and ice sheets*, measurements for those two classes are calculated to have a weight of 813.9 (Fig. 2). Other underrepresented tectono-geographical regions include, as a most recent orogen, the Birimian Orogen, Kuunga Orogen and particularly the Scotian Orogen, where no heat flow measurements are catalogued. Generally, Gondwana and the oceanic crust are underrepresented.

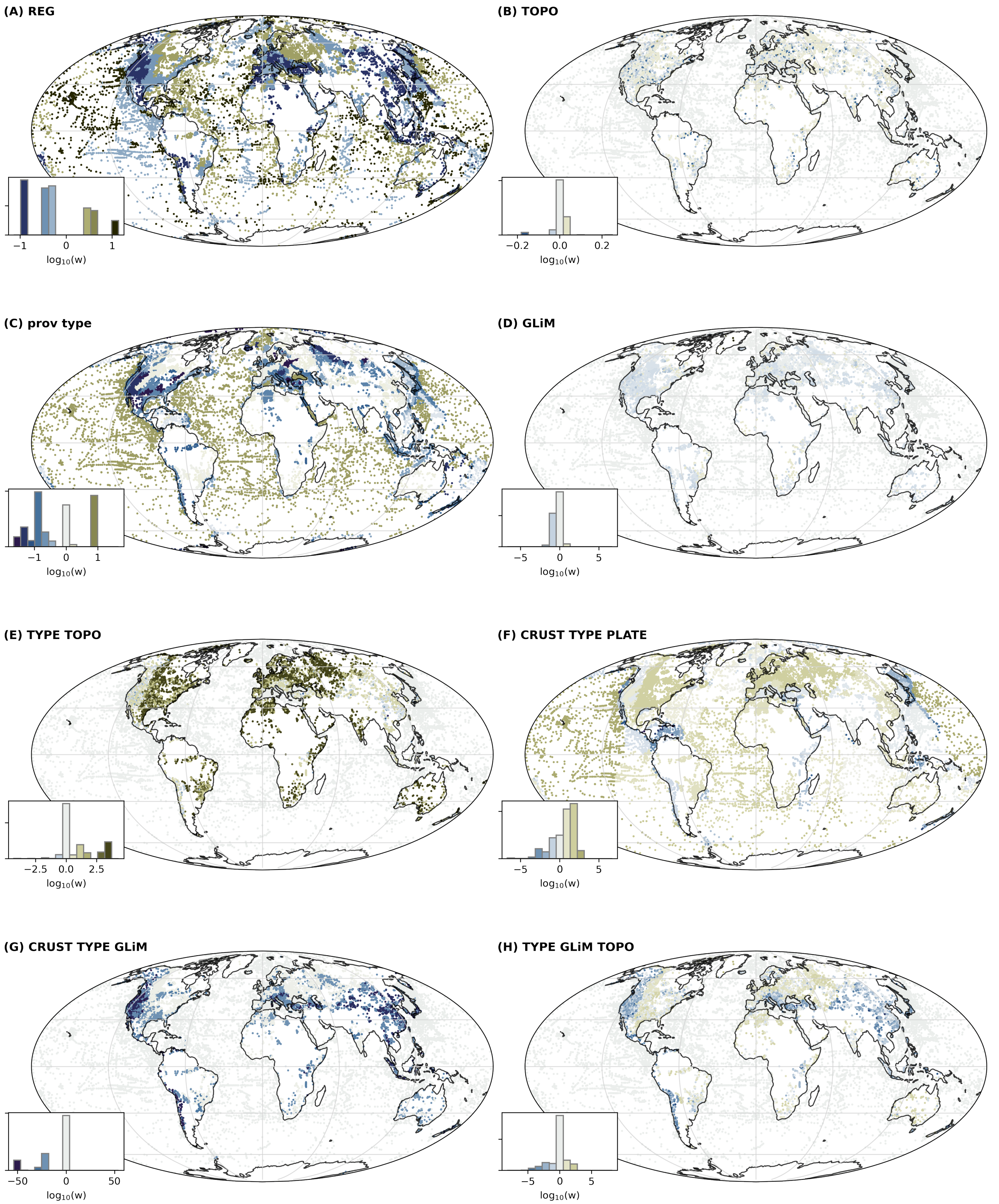

Figure 4. (Caption next page.)

Figure 4. Calculated weights for selected categorical variables and suggestions for combined weights. **(A)** REG (Schaeffer and Lebedev, 2015) **(B)** Geomorphological forms (Amatulli et al., 2020) **(C)** Province (Hasterok et al., 2022) **(D)** GLiM (Hartmann and Moosdorf, 2012) **(E)** IPF calculated joint weighting from TYPE and TOPO, **(F)** IPF calculated joint weighting from CRUST, TYPE, and PLATE, **(G)** IPF calculated joint weighting from TYPE and GLiM, **(H)** IPF calculated joint weighting from TYPE, GLiM, and TOPO. The weights are displayed as a logarithmic colour representation, with weight (1, no weighting applied) in grey, blue indicates that the measurements are weighted down, and brown indicates that the measurements are weighted up. The inset histogram shows the relative log–value distribution. Note that the scale differs for each subplot for clarity.

4 DISCUSSION

We have shown that the distribution of heat flow measurements is spatially biased and does not fully represent the Earth's geometric, tectonic, geological or geomorphometric disposition. This conclusion is readily seen from the clustering of measurements (Fig. 1), and in the context of eight auxiliary variables, whereby we found that some settings are overrepresented whilst others are correspondingly underrepresented. The selection of those variables is somewhat arbitrary; however, together, they represent a meaningful range of parameters that should be expected to impact the distribution of geothermal heat.

The calculated weights from each variable compensate for the bias, and the combined fitted weights provide individually optimised weights for each record in IHFC. The somewhat diverging results highlight the need for caution when weighting is applied in empirical models. The choice of weights depends on the scale of the model and relevence of the variables used. It would be tempting to evaluate the weights based on their performance to reduce prediction misfits in existing empiric models; however, such an appraisal will necessarily contain the same bias. A useful test case could be cross-validation of a sufficiently large subset of the heat flow catalogue that can be shown to truly represent a random sampling of the Earth, and of good quality. Unfortunately, given that some settings are strongly underrepresented, such a sample distribution is not yet possible. With empirically driven heat flow models, there is potential to further explore how the weighting and processing of reference measurements can impact the results. Some observables, such as the distance to volcanoes, have been shown to have large impact (Lösing and Ebbing, 2021); however, the sensitivity changes if weights are applied, and in many cases extreme geothermal settings are weighted down.

One potential shortcoming in this study is that we have assumed that the coordinates of the measurements are given correctly and accurately to match the auxiliary variables; this is often not the case. The surprisingly low bias in the geomorphometrics variable might be, at least partially, explained by imprecise positions that sample random geomorphological forms in the vicinity rather than the actual topographic shape right at the borehole.

From an assumption that weighted mean and median values from the catalogue should approach the qualitative estimates of the global heat flow distribution, the closest weighted mean is given precedence in our interpretation. The total Earth heat loss is estimated to be 40–42 TW, or 80 $\mathrm{mW\,m^{-2}}$ (Lucazeau, 2019). Earlier studies come to similar results (e.g. Pollack et al., 1993). Most weighted mean values are closer to this average, suggesting that weight applied to metrics of the catalogue can improve the prediction if applied carefully.

Weights derived from one auxiliary variable, that generate weighted averages close to the expected global value: Last orogeny (OROGEN) average is +12 $\mathrm{mW\,m^{-2}}$ compared to global average, shallow geology (GLiM), +13 $\mathrm{mW\,m^{-2}}$, geomorphometric shapes (TOPO), +26 $\mathrm{mW\,m^{-2}}$, and tectonic plate, +26 $\mathrm{mWm^{-2}}$.

The fitted weight from plate type (TYPE) and topography (TOPO) (Fig. 4E) produces a close value of +4 mWm^{-2}, however we have concerns regarding the validity of the geomorphometrics (TOPO), as the coordinates given in the catalogue might not be precise enough. Moreover, marine data is note weighted to topography. Plate type (TYPE) and shallow geology (GLiM) also generate a weighting that is similar to the global average at +16 mWm^{-2} (Fig. 4G). Qualitative reasoning of what processes impact heat flow would on different scales, weighting for tectonic setting (TYPE), shallow geology (GLiM) and topography (TOPO) gives a weighted mean difference of +65 mWm^{-2} (Fig. 4H).

The spatial sampling bias is consistent with the challenges and lack of incentives to conduct investigations in remote regions or developing countries. More measurements of the thermal gradient have likely been conducted for prospecting and exploration reasons in some of such sparse areas; however, the results are not included in heat flow compilations and the understanding of some areas suffers from very sparse records (Fig. 1C-D, Brigaud et al. (Discussed and extended by e.g. 1985); Lesquer and Vasseur (Discussed and extended by e.g. 1992); Noorollahi et al. (Discussed and extended by e.g. 2009); Yousefi et al. (Discussed and extended by e.g. 2010)).

Acknowledging the achievement of the cumulative heat flow catalogues, the scope of this contribution is to support and add value to the ongoing, substantial undertaking to coordinate a representative compilation of measurements.

We make six recommendations from the results of this study:

1. Empirical heat flow model developers should consider applying weights when using the reference database and investigate how this can reduce uncertainty and misfit.
2. The spatial coordinates of heat flow measurements should, whenever possible, be amended such that they are sufficiently precise and accurate to facilitate statistical analysis of refraction from topography and shallow geology. This is viable thanks to the availability of global high resolution digital elevation model and refined geological maps.
3. Attribute data could be added to heat flow records, including information about geological setting and uncertainties, to assist in future appraisals.
4. In the ongoing assessment project of the IHFC database, highly weighted existing records should be assessed first, as they represent underrepresented settings.
5. Underrepresented regions and settings should be prioritised when new data is incorporated into IHFC.
6. To truly improve the global thermal representation of the catalogue, underrepresented regions and settings should be prioritised for future new heat flow measurements, particularly within the Gondwanan continents Antarctica, Africa, and Australia; and particularly in regions without an immediate interest for mineral or hydrocarbon exploration.

CONFLICT OF INTEREST STATEMENT

The authors declare that the research was conducted in the absence of any commercial or financial relationships that could be construed as a potential conflict of interest.

AUTHOR CONTRIBUTIONS

TS conceived the presented idea, developed the theory and performed the computations. AR and RT verified and advised on the analytical methods. AR, SF, JH and ML supervised the findings of this work. All authors discussed the results and contributed to the final manuscript.

FUNDING

This research was supported by the Australian Research Council through ARC DP190100418, ARC Special Research Initiative, Australian Centre for Excellence in Antarctic Science (Project Number SR200100008), and ARC DP180104074. Additional support was provided through the Deutsche Forschungsgemeinschaft (DFG) in the framework of the priority programme "Antarctic Research with comparative investigations in Arctic ice areas" (Grant No. EB 255/8-1).

ACKNOWLEDGMENTS

We thank Matthew Cracknell and Nick Direen for their insights into ore prospecting and spatial datasets of mining sites. Discussions informing this review were facilitated by the Scientific Committee on Antarctic Research, Instabilities and Thresholds in Antarctica, sub-committee on Geothermal Heat Flow (SCAR, INSTANT).

SUPPLEMENTAL DATA

Additional details regarding the analysis and a table containing the extracted observable layers are provided as supplementary material.

DATA AVAILABILITY STATEMENT

Observables sampled at each location of heat flow measurements listed in IHFC (www.ihfc-iugg.org), weights, and combined weights generated in this study can be found in the `url_to_zenodo`. The values can be joined to the IHFC database with the ID number. For clarity, the database also contains selected columns from IHFC. The database is provided and stored in Excel, parquet and GIS formats. We also share the table of variables. The Python code used to produce this study is available at `https://github.com/TobbeTripitaka/heat-flow-sampling-bias` and achieved at `url_to_zenodo`. Links to all datasets used as auxiliary variables are also provided with the code.

REFERENCES

Amatulli, G., Domisch, S., Tuanmu, M. N., Parmentier, B., Ranipeta, A., Malczyk, J., et al. (2018). Data Descriptor: A suite of global, cross-scale topographic variables for environmental and biodiversity modeling. *Scientific Data* 5, 1–15. doi:10.1038/sdata.2018.40

Amatulli, G., McInerney, D., Sethi, T., Strobl, P., and Domisch, S. (2020). Geomorpho90m, empirical evaluation and accuracy assessment of global high-resolution geomorphometric layers. *Scientific Data* 7, 1–18. doi:10.1038/s41597-020-0479-6

An, M., Wiens, D. A., Zhao, Y., Feng, M., Nyblade, A., Kanao, M., et al. (2015). Temperature, lithosphere-asthenosphere boundary, and heat flux beneath the Antarctic Plate inferred from seismic velocities. *Journal of Geophysical Research: Solid Earth* 120, 8720–8742. doi:10.1002/2015JB011917

Artemieva, I. M. (2022). Antarctica ice sheet basal melting enhanced by high mantle heat. *Earth-Science Reviews* 226, 103954. doi:10.1016/j.earscirev.2022.103954

Bahadori, A., Zendehboudi, S., Zahedi, G., et al. (2013). A review of geothermal energy resources in australia: current status and prospects. *Renewable and Sustainable Energy Reviews* 21, 29–34

Beardsmore, G. R. and Cull, J. P. (2001). *Crustal Heat Flow* (Press, Cambridge University). doi:10.1017/cbo9780511606021

Brigaud, F., Lucazeau, F., Ly, S., and Sauvage, J. F. (1985). Heat flow from the west african shield. *Geophysical Research Letters* 12, 549–552

Burton-Johnson, A., Dziadek, R., and Martin, C. (2020). Geothermal heat flow in Antarctica: current and future directions. *The Cryosphere Discussions* 14, 1–45. doi:10.5194/tc-2020-59

Burton-Johnson, A., Halpin, J. A., Whittaker, J. M., Graham, F. S., and Watson, S. J. (2017). A new heat flux model for the Antarctic Peninsula incorporating spatially variable upper crustal radiogenic heat production. *Geophysical Research Letters* 44, 5436–5446. doi:10.1002/2017GL073596

Colgan, W., Wansing, A., Mankoff, K., Lösing, M., Hopper, J., Louden, K., et al. (2022). Greenland Geothermal Heat Flow Database and Map (Version 1). *Earth System Science Data* 14, 2209–2238. doi:10.5194/essd-14-2209-2022

[Dataset] Crameri, F. and Shephard, G. E. (2019). Scientific Colour Maps. doi:10.5281/zenodo.3596401

Cull, J. P., Houseman, G. A., Muir, P. M., and Paterson, H. L. (1988). Geothermal Signatures and Uranium Ore Deposits on the Stuart Shelf of South Australia. *Exploration Geophysics* 19, 34–38. doi:10.1071/EG988034

Davies, J. H. and Davies, D. R. (2010). Earth's surface heat flux. *Solid Earth* 1, 5–24. doi:10.5194/se-1-5-2010

Dickson, M. H. and Fanelli, M. (2013). *Geothermal energy: utilization and technology* (Routledge)

Dixon, P. M. (2014). Ripley's K Function. *Wiley StatsRef: Statistics Reference Online* 3, 1796–1803. doi:10.1002/9781118445112.stat07751

Ebbing, J., Gernigon, L., Pascal, C., Olesen, O., and Osmundsen, P. T. (2009). A discussion of structural and thermal control of magnetic anomalies on the mid-Norwegian margin. *Geophysical Prospecting* 57, 665–681. doi:10.1111/j.1365-2478.2009.00800.x

[Dataset] Forthommme, D. (2021). Iterative Proportional Fitting for Python with N Dimensions

Fuchs, S., Beardsmore, G., Chiozzi, P., Espinoza-Ojeda, O. M., Gola, G., Gosnold, W., et al. (2021a). A new database structure for the IHFC Global Heat Flow Database. *International Journal of Terrestrial Heat Flow and Applications* 4, 1–14. doi:10.31214/ijthfa.v4i1.62

Fuchs, S., Norden, B., and Commission, I. H. F. (2021b). The Global Heat Flow Database: Release 2021. GFZ Data Services, 1–73. doi:10.5880/fidgeo.2021.014

Gard, M. and Hasterok, D. (2021). A global Curie depth model utilising the equivalent source magnetic dipole method. *Physics of the Earth and Planetary Interiors* 313, 106672. doi:10.1016/j.pepi.2021.106672

Gillies, S. (2019). rasterio Documentation

Goes, S., Hasterok, D., Schutt, D. L., and Klöcking, M. (2020). Continental lithospheric temperatures: A review. *Physics of the Earth and Planetary Interiors* 306. doi:10.1016/j.pepi.2020.106509

Goutorbe, B., Poort, J., Lucazeau, F., and Raillard, S. (2011). Global heat flow trends resolved from multiple geological and geophysical proxies. *Geophysical Journal International* 187, 1405–1419. doi:10.1111/j.1365-246X.2011.05228.x

Greve, R. and Hutter, K. (1995). Polythermal three-dimensional modelling of the Greenland ice sheet with varied geothermal heat flux. *Annals of Glaciology* 21, 8–12. doi:10.3189/S0260305500015524

Haeger, C., Kaban, M. K., Tesauro, M., Petrunin, A. G., and Mooney, W. D. (2019). 3-D Density, Thermal, and Compositional Model of the Antarctic Lithosphere and Implications for Its Evolution. *Geochemistry, Geophysics, Geosystems* 20, 688–707. doi:10.1029/2018GC008033

Harris, C. R., Millman, K. J., van der Walt, S. J., Gommers, R., Virtanen, P., Cournapeau, D., et al. (2020). Array programming with NumPy. *Nature* 585, 357–362. doi:10.1038/s41586-020-2649-2

Hartmann, J. and Moosdorf, N. (2012). The new global lithological map database GLiM: A representation of rock properties at the Earth surface. *Geochemistry, Geophysics, Geosystems* 13, 1–37. doi:10.1029/2012GC004370

Hasterok, D. and Gard, M. (2016). Utilizing thermal isostasy to estimate sub-lithospheric heat flow and anomalous crustal radioactivity. *Earth and Planetary Science Letters* 450, 197–207. doi:10.1016/j.epsl.2016.06.037

Hasterok, D., Gard, M., and Webb, J. (2018). On the radiogenic heat production of metamorphic, igneous, and sedimentary rocks. *Geoscience Frontiers* 9, 1777–1794. doi:10.1016/j.gsf.2017.10.012

Hasterok, D., Halpin, J., Collins, A., Hand, M., Kreemer, C., Gard, M., et al. (2022). New maps of global geological provinces and tectonic plates. *Earth-Science Reviews* , 104069doi:https://doi.org/10.1016/j.earscirev.2022.104069

Holgate, F. L., Goh, H. K., Wheller, G., and Lewis, R. G. (2010). The Central Tasmanian geothermal anomaly: A prospective new EGS province in Australia. In *Proceedings World Geothermal Congress, Bali, Indonesia*. 1–6

Huang, S., Pollack, H. N., and Shen, P. Y. (1997). Late Quaternary temperature changes seen in world-wide continental heat flow measurements. *Geophysical Research Letters* 24, 1947–1950. doi:10.1029/97GL01846

Hunter, J. D. (2007). Matplotlib: A 2D graphics environment. *Computing in Science and Engineering* 9, 99–104. doi:10.1109/MCSE.2007.55

Jasiewicz, J. and Stepinski, T. F. (2013). Geomorphons-a pattern recognition approach to classification and mapping of landforms. *Geomorphology* 182, 147–156. doi:10.1016/j.geomorph.2012.11.005

Jaupart, C., Mareschal, J. C., and Iarotsky, L. (2016). Radiogenic heat production in the continental crust. *Lithos* 262, 398–427. doi:10.1016/j.lithos.2016.07.017

Jordahl, K. (2014). GeoPandas: Python tools for geographic data. *URL: https://github.com/geopandas/geopandas*

Kalton, G. and Flores-Cervantes, I. (2003). Weighting Methods. *Journal of Official Statistics* 19, 81–97

Karlsson, N. B., Solgaard, A. M., Mankoff, K. D., Gillet-Chaulet, F., MacGregor, J. A., Box, J. E., et al. (2021). A first constraint on basal melt-water production of the Greenland ice sheet. *Nature Communications* 12, 1–10. doi:10.1038/s41467-021-23739-z

Kelvin, W. T. (1863). On the secular cooling of the earth. *Transactions of the Royal Society of Edinburgh* 23, 157–170

Lees, C. H. C. H., Districts, R.-a., and Lees, C. H. C. H. (1910). On the shapes of the isogeotherms under mountain ranges in radio-active districts. *Proceedings of the Royal Society of London. Series A, Containing Papers of a Mathematical and Physical Character* 83, 339–346. doi:10.1098/rspa.1910.0022

Lesquer, A. and Vasseur, G. (1992). Heat-flow constraints on the West African lithosphere structure. *Geophysical Research Letters* 19, 561–564. doi:10.1029/92GL00263

Li, M., Huang, S., Dong, M., Xu, Y., Hao, T., Wu, X., et al. (2021). Prediction of marine heat flow based on the random forest method and geological and geophysical features. *Marine Geophysical Research* 42. doi:10.1007/s11001-021-09452-y

Lösing, M. and Ebbing, J. (2021). Predicting Geothermal Heat Flow in Antarctica With a Machine Learning Approach. *Journal of Geophysical Research: Solid Earth* 126, 1–32. doi:10.1029/2020JB021499

Lösing, M., Ebbing, J., and Szwillus, W. (2020). Geothermal Heat Flux in Antarctica: Assessing Models and Observations by Bayesian Inversion. *Frontiers in Earth Science* 8, 1–13. doi:10.3389/feart.2020.00105

Lucazeau, F. (2019). Analysis and Mapping of an Updated Terrestrial Heat Flow Data Set. *Geochemistry, Geophysics, Geosystems* 20, 4001–4024. doi:10.1029/2019GC008389

Mansure, A. J. and Reiter, M. (1979). A vertical groundwater movement correction for heat flow. *Journal of Geophysical Research: Solid Earth* 84, 3490–3496. doi:10.1029/JB084iB07p03490

Martos, Y. M., Catalán, M., Jordan, T. A., Golynsky, A., Golynsky, D., Eagles, G., et al. (2017). Heat Flux Distribution of Antarctica Unveiled. *Geophysical Research Letters* 44, 11,417–11,426. doi:10.1002/2017GL075609

Maus, V., Giljum, S., Gutschlhofer, J., da Silva, D. M., Probst, M., Gass, S. L., et al. (2020). A global-scale data set of mining areas. *Scientific Data* 7, 1–13. doi:10.1038/s41597-020-00624-w

Morse, P. E., Reading, A. M., and Stål, T. (2019). Well-Posed Geoscientific Visualization Through Interactive Color Mapping. *Frontiers in Earth Science* 7, 0–17. doi:10.3389/feart.2019.00274

Noorollahi, Y., Yousefi, H., Itoi, R., and Ehara, S. (2009). Geothermal energy resources and development in iran. *Renewable and Sustainable Energy Reviews* 13, 1127–1132. doi:https://doi.org/10.1016/j.rser.2008.05.004

Pasquale, V., Verdoya, M., and Chiozzi, P. (2014). *SPRINGER BRIEFS IN EARTH SCIENCES Geothermics Heat Flow in the Lithosphere*

Pattyn, F. (2010). Antarctic subglacial conditions inferred from a hybrid ice sheet/ice stream model. *Earth and Planetary Science Letters* 295, 451–461. doi:10.1016/j.epsl.2010.04.025

Pollack, H. N., Hurter, S. J., and Johnson, J. R. (1993). Heat flow from the Earth's interior: Analysis of the global data set. *Reviews of Geophysics* 31, 267–280. doi:10.1029/93RG01249

Rose, K., Bauer, J., Baker, V., Barkhurst, A., Bean, A., DiGiulio, J., et al. (2018). *Global Oil & Gas Features Database*. Tech. rep., National Energy Technology Laboratory (NETL), Pittsburgh, PA, Morgantown, WV ...

Royden, L. and Sclater, J. G. (1980). Continental Margin Subsidence and Heat Flow: Important Parameters in Formation of Petroleum Hydrocarbons. *AAPG Bulletin* 64. doi:10.1306/2F91894B-16CE-11D7-8645000102C1865D

Šafanda, J., Szewczyk, J., and Majorowicz, J. (2004). Geothermal evidence of very low glacial temperatures on a rim of the Fennoscandian ice sheet. *Geophysical Research Letters* 31, 4–7. doi:10.1029/2004GL019547

Schaeffer, A. J. and Lebedev, S. (2015). Global heterogeneity of the lithosphere and underlying mantle: A seismological appraisal based on multimode surface-wave dispersion analysis, shear-velocity tomography, and tectonic regionalization. In *The Earth's Heterogeneous Mantle: A Geophysical, Geodynamical, and Geochemical Perspective* (Springer International Publishing). 3–46. doi:10.1007/978-3-319-15627-9_1

Shalaby, M. R., Hakimi, M. H., and Abdullah, W. H. (2011). Geochemical characteristics and hydrocarbon generation modeling of the jurassic source rocks in the shoushan basin, north western desert, egypt. *Marine and Petroleum Geology* 28, 1611–1624. doi:10.1016/j.marpetgeo.2011.07.003

Shen, W., Wiens, D. A., Lloyd, A. J., and Nyblade, A. A. A. (2020). A Geothermal Heat Flux Map of Antarctica Empirically Constrained by Seismic Structure. *Geophysical Research Letters* 47, 0–2. doi:10.1029/2020GL086955

Stål, T. (2022). Fast calculation of Ripley's K and L functions on a sphere. *In prep.*

Stål, T. and Reading, A. M. (2020). A Grid for Multidimensional and Multivariate Spatial Representation and Data Processing. *Journal of Open Research Software* 8, 1–10. doi:10.5334/jors.287

Stål, T., Reading, A. M., Halpin, J. A., Phipps, S. J., Whittaker, J. M., Steven J, P., et al. (2020a). The Antarctic Crust and Upper Mantle: A Flexible 3D Model and Software Framework for Interdisciplinary Research. *Frontiers in Earth Science* 8, 1–19. doi:10.3389/feart.2020.577502

Stål, T., Reading, A. M., Halpin, J. A., and Whittaker, J. M. (2020b). Antarctic geothermal heat flow model: Aq1. *Geochemistry, Geophysics, Geosystems* 22, 1–22. doi:10.1029/2020GC009428

Von Herzen, R. P. and Uyeda, S. (1963). Heat flow through the eastern Pacific ocean floor. *Journal of Geophysical Research* 68, 4219–4250. doi:10.1029/JZ068i014p04219

Yamazaki, D., Ikeshima, D., Tawatari, R., Yamaguchi, T., O'Loughlin, F., Neal, J. C., et al. (2017). A high-accuracy map of global terrain elevations. *Geophysical Research Letters* 44, 5844–5853. doi:10.1002/2017GL072874

Yousefi, H., Noorollahi, Y., Ehara, S., Itoi, R., Yousefi, A., Fujimitsu, Y., et al. (2010). Developing the geothermal resources map of iran. *Geothermics* 39, 140–151. doi:https://doi.org/10.1016/j.geothermics.2009.11.001

SUPPLEMENTARY MATERIAL

COMMENTS TO PREPRINT AND DATA AVAILABILITY

Attached with this contribution is a version of the recent compilation of IUGG IHFC with added attributes from observables and calculated weights added as attributes (Fuchs et al., 2021b). The catalogue will be provided in well-known formats (Excel and text), fast readable binary format (Parquet), as well as GIS readable formats (Geopackage, Shapefiles). The compiled results are also provided in JSON and parquet formats.

For the mean time, awaiting review of dataset and paper, the catalogue is temporary provided at DOI: `https://zenodo.org/record/6626377`, however please contact `tobias.staal@utas.edu.au` to ensure you get the latest version.

Code used to produce this paper is available from: `https://github.com/TobbeTripitaka/heat-flow-sampling-bias`. The code will be reformatted and further commented.

5 SUPPLEMENTARY TABLES AND FIGURES

5.1 Tables

variable	category	weight	q mean	q median	p1 mean	p10 mean
REG			**151.01**	**65.35**	**90.29**	**69.36**
Fig. 2A	cratons	1.73	0.056	0.054		
	belts and mod. crt.	0.63	0.060	0.055		
	phanerozoic	0.37	0.209	0.076		
	ridges and backarcs	0.69	0.529	0.113		
	oceanic	3.12	0.080	0.060		
	old oceanic	1.69	0.061	0.048		
PROVINCE			**309.80**	**73.41**	**131.67**	**77.48**
Fig. 2B	orogenic belt	1.05	0.073	0.066		
	shield	1.12	0.070	0.059		
	craton	1.12	0.052	0.050		
	volcanic arc	0.45	0.134	0.063		
	oceanic crust	2.25	0.477	0.082		
	narrow rift	0.34	0.107	0.069		
	foredeep basin	1.15	0.085	0.085		
	passive margin	0.55	0.060	0.053		
	ophiolite complex	1.28	0.060	0.051		
	accretionary cmplx.	0.40	0.063	0.044		
	basin	1.23	0.065	0.062		
	back-arc basin	0.65	0.312	0.080		
	wide rift	0.24	0.238	0.099		
	magmatic province	0.19	0.099	0.048		
	oceanic back-arc bsn.	0.91	0.100	0.086		
CRUST			**319.32**	**74.51**	**134.05**	**79.33**
Fig. 2C	continental	0.61	0.101	0.063		
	oceanic	2.12	0.471	0.084		
	transitional	0.44	0.111	0.052		
TYPE			**214.09**	**62.43**	**104.17**	**71.69**
Fig. 2D	microplate	0.44	0.137	0.067		
	rigid plate	1.33	0.221	0.060		
	deform. zone	0.43	0.226	0.081		
PLATE			**106.33**	**67.53**	**89.13**	**75.81**
Fig. 2E	Eurasian	0.54	0.100	0.063		
	Arabian	1.02	0.115	0.083		
	Pacific	3.76	0.098	0.062		
	N. American	0.29	0.137	0.063		
	Antarctic	15.30	0.095	0.075		
	Nazca	1.41	0.300	0.195		
	Scotia	8.31	0.111	0.102		
	Australian	3.58	0.068	0.061		
	S. American	2.95	0.073	0.061		
	Philippine	0.65	0.639	0.075		
	Caribbean	0.15	0.047	0.040		
	Juan de Fuca	0.01	1.694	0.324		
	Cocos	0.50	0.107	0.066		
	African	1.78	0.077	0.057		
	Somali	4.41	0.071	0.058		
	Indian	3.16	0.066	0.062		
OROGEN			**92.25**	**63.32**	**101.23**	**72.75**

Table S1. Continues next page.

variable	category	weight	q mean	q median	p1 mean	p10 mean
Fig. 2F	Kuunga	10.35	0.057	0.055		
	Yavapai-Mazatzal	1.44	0.055	0.051		
	Trans Hudson	1.42	0.056	0.057		
	Limpopo	7.48	0.055	0.055		
	cratonic	1.93	0.052	0.050		
	East African	3.94	0.056	0.050		
	Variscan-Hercynian	0.40	0.067	0.062		
	Birimian	13.32	0.053	0.047		
	Grenvillian	0.73	0.061	0.061		
	Brasiliano	2.33	0.071	0.066		
	Afar	0.46	0.135	0.119		
	Alpine-Himalayan	0.78	0.071	0.065		
	Terra Australis	4.68	0.067	0.062		
	Saharide	5.78	0.078	0.076		
	Cordilleran	0.63	0.224	0.085		
	failed rift	1.20	0.052	0.051		
	Kazakh	1.51	0.052	0.050		
	Baikal	0.02	0.097	0.074		
	Mongol	2.23	0.063	0.056		
	Indosinian	1.33	0.091	0.083		
	Solonker	4.07	0.069	0.071		
	Caledonian	0.84	0.065	0.061		
	Uralian	2.08	0.034	0.030		
	Picuris	0.19	0.048	0.046		
	Wopmay	0.20	0.069	0.066		
	Antilles	0.16	0.046	0.040		
	Scotian	inf	nan	nan		
GLiM			**93.34**	**65.13**	**104.62**	**76.26**
Fig. 2G	unconsolidated sed.	0.51	0.105	0.062		
	siliciclastic sed.	0.60	0.083	0.062		
	mixed sed.	0.94	0.069	0.059		
	carbonate sed.	1.00	0.076	0.054		
	pyroclastic	0.38	0.221	0.100		
	evaporites	2.38	0.042	0.041		
	metamorphics	2.23	0.105	0.064		
	basic volcanic	0.43	0.179	0.083		
	inter. volcanic	0.67	0.109	0.077		
	acid volcanic	0.21	0.241	0.113		
	basic plutonic	2.50	0.057	0.050		
	inter. plutonic	1.36	0.071	0.060		
	acid plutonic	1.08	0.136	0.063		
	water Bodies	0.28	0.111	0.062		
	ice and Glaciers	813.87	0.081	0.072		
	no data	1.00	0.070	0.069		
TOPO			**105.56**	**63.10**	**107.11**	**74.08**
Fig. 2H	flat	1.03	0.086	0.060		
	peak	1.12	0.092	0.063		
	ridge	0.99	0.095	0.065		

Table S1. Continues next page.

variable	category	weight	q mean	q median	p1 mean	p10 mean
	shoulder	0.86	0.083	0.060		
	spur	0.98	0.130	0.067		
	slope	1.01	0.136	0.066		
	hollow	0.95	0.115	0.067		
	valley	0.95	0.107	0.066		
	pit	1.28	0.129	0.069		
Mines			**210.07**	**63.96**	**107.70**	**73.88**
Fig. 3A	No mine	1.06	0.212	0.064		
	mine	0.24	0.126	0.067		
Oil and gas fields			**229.50**	**64.90**	**114.42**	**75.55**
Fig. 3A	No oil gas	1.18	0.235	0.065		
	oil gas	0.19	0.067	0.062		

Table S1. Auxiliary variable classes. Heat flow values are given in mWm^{-2}. p1 excludes the upper and lower 1% percentiles, p10 excludes the upper and lower 10% percentiles from the calculation of the mean. Bold values refer to the weighted calculation from the auxiliary variable.

	label_1	label_2	label_3	label_4	flag	q_mean	q_median	Diff
0	TYPE	TOPO			1	84.05	58.00	3.67
1	TYPE	PLATE			1	95.27	59.00	14.89
2	TYPE	GLiM			1	96.62	58.20	16.24
3	PLATE	REG			1	105.46	59.00	25.08
4	CRUST	PLATE			1	107.96	62.80	27.58
5	PROVINCE	PLATE			1	113.76	62.00	33.38
6	CRUST	TOPO			1	115.53	62.00	35.15
7	REG	TOPO			1	127.45	60.00	47.07
8	GLiM	TOPO			1	136.32	61.00	55.94
9	PLATE	TOPO			1	139.00	62.00	58.62
10	OROGEN	TYPE			1	147.44	62.00	67.06
11	REG	GLiM			1	147.63	61.00	67.25
12	PLATE	GLiM			1	158.10	62.00	77.72
13	OROGEN	PLATE			1	174.16	66.00	93.78
14	PROVINCE	TOPO			1	175.51	63.00	95.13
15	PROVINCE	OROGEN			1	178.98	64.00	98.60
16	OROGEN	REG			1	180.23	66.00	99.85
17	OROGEN	TOPO			1	193.26	68.00	112.88
18	TYPE	REG			1	201.88	60.00	121.50
19	OROGEN	GLiM			1	204.75	66.00	124.37
20	CRUST	GLiM			1	219.17	62.00	138.79
21	CRUST	REG			1	238.87	63.00	158.49
22	PROVINCE	GLiM			1	301.81	67.00	221.42
23	OROGEN	CRUST			1	302.64	58.40	222.26
24	CRUST	TYPE			1	306.60	65.00	226.22
25	PROVINCE	REG			1	357.32	68.00	276.94
26	PROVINCE	CRUST			1	419.79	75.00	339.41
27	PROVINCE	TYPE			1	433.24	70.00	352.86

Table S2. Iterative proportional fitting of all pairs of auxiliary variables. Flag indicates converging matrix (1), or maximum iterations (N = 500) reached (0). We use the calculated weight to compute a weighted mean and a weighted median value. The table is sorted according to the difference from the estimated average global heat flow from Lucazeau (2019). The small difference is not an argument for the selected weighting variables, however, large differences are not likely to improve estimates using the here presented weights. Mean of IHFC - global average (Lucazeau, 2019) is 124 $mW\,m^{-2}$. The mean of all calculated difference values is 114 $mW\,m^{-2}$

	label_1	label_2	label_3	label_4	flag	q_mean	q_median	Diff
0	CRUST	TYPE	PLATE		1	93.42	60.00	13.04
1	TYPE	PLATE	REG		1	95.95	58.00	15.57
2	CRUST	PLATE	REG		1	102.95	59.00	22.57
3	CRUST	TYPE	TOPO		1	107.31	58.30	26.92
4	PROVINCE	TYPE	PLATE		1	107.44	60.00	27.06
5	PROVINCE	CRUST	PLATE		1	114.94	62.00	34.56
6	PROVINCE	PLATE	REG		1	124.93	62.00	44.55
7	TYPE	REG	TOPO		1	126.16	58.00	45.78
8	TYPE	PLATE	TOPO		1	137.84	59.00	57.46
9	TYPE	GLiM	TOPO		1	145.23	59.00	64.85
10	TYPE	REG	GLiM		1	150.20	59.00	69.81
11	CRUST	REG	TOPO		1	158.97	59.00	78.59
12	TYPE	PLATE	GLiM		1	167.21	59.00	86.83
13	PROVINCE	OROGEN	TYPE		1	167.50	59.00	87.12
14	CRUST	TYPE	GLiM		1	168.96	59.00	88.58
15	OROGEN	CRUST	TYPE		1	182.13	58.00	101.75
16	OROGEN	TYPE	REG		1	182.60	61.00	102.22
17	OROGEN	TYPE	PLATE		1	184.60	63.20	104.22
18	OROGEN	TYPE	TOPO		1	188.87	62.00	108.49
19	PLATE	REG	TOPO		1	195.08	61.00	114.70
20	PROVINCE	TYPE	TOPO		1	195.98	62.00	115.59
21	CRUST	PLATE	TOPO		1	196.17	64.00	115.79
22	OROGEN	CRUST	TOPO		1	205.02	59.00	124.64
23	PLATE	GLiM	TOPO		1	207.75	62.00	127.37
24	OROGEN	TYPE	GLiM		1	212.39	63.00	132.01
25	PROVINCE	CRUST	TOPO		1	213.17	64.00	132.79
26	PROVINCE	OROGEN	REG		1	217.20	62.00	136.82
27	PLATE	REG	GLiM		1	220.47	60.00	140.09
28	REG	GLiM	TOPO		1	221.61	61.00	141.23
29	CRUST	GLiM	TOPO		1	222.40	62.00	142.02
30	OROGEN	PLATE	REG		1	223.56	65.00	143.18
31	PROVINCE	OROGEN	TOPO		1	226.15	63.00	145.77
32	PROVINCE	REG	TOPO		1	227.16	62.00	146.78
33	OROGEN	REG	TOPO		1	232.94	65.20	152.56
34	OROGEN	PLATE	TOPO		1	234.27	65.00	153.89
35	PROVINCE	OROGEN	GLiM		1	241.60	65.00	161.22
36	OROGEN	PLATE	GLiM		1	248.17	64.00	167.79
37	CRUST	TYPE	REG		1	250.75	61.00	170.36
38	OROGEN	CRUST	REG		1	252.03	58.00	171.65
39	OROGEN	REG	GLiM		1	253.42	66.00	173.04
40	OROGEN	GLiM	TOPO		1	257.33	65.00	176.95
41	CRUST	PLATE	GLiM		1	266.59	65.00	186.21
42	PROVINCE	PLATE	TOPO		1	269.52	65.20	189.14
43	OROGEN	CRUST	GLiM		1	284.61	63.40	204.23
44	PROVINCE	CRUST	GLiM		1	293.62	65.00	213.24
45	PROVINCE	GLiM	TOPO		1	293.63	66.00	213.24
46	CRUST	REG	GLiM		1	311.66	65.00	231.27
47	PROVINCE	TYPE	GLiM		1	312.35	67.00	231.97
48	PROVINCE	PLATE	GLiM		1	317.55	66.00	237.17
49	OROGEN	CRUST	PLATE		1	318.66	69.00	238.28
50	PROVINCE	TYPE	REG		1	362.96	66.00	282.57
51	PROVINCE	CRUST	REG		1	370.82	70.00	290.44
52	PROVINCE	OROGEN	CRUST		1	417.29	60.00	336.91
53	PROVINCE	CRUST	TYPE		1	453.28	73.00	372.90
54	PROVINCE	OROGEN	PLATE		0	292.82	68.00	212.44
55	PROVINCE	REG	GLiM		0	310.06	68.00	229.68

Table S3. Iterative proportional fitting of all triples of auxiliary variables. Flag indicates converging matrix (1), or maximum iterations (N = 500) reached (0). We use the calculated weight to compute a weighted mean and a weighted median value. The table is sorted according to difference from estimated average global heat flow from Lucazeau (2019). Small difference is itself not an argument for the selected weighting variables, however large differences are not likely to improve estimates using the here presented weights. Mean of IHFC - global average (Lucazeau, 2019) is 124 $mW\,m^{-2}$. The mean of all calculated difference values is 114 $mW\,m^{-2}$

	label_1	label_2	label_3	label_4	flag	q_mean	q_median	Diff
0	CRUST	TYPE	PLATE	REG	1	94.80	58.00	14.42
1	PROVINCE	CRUST	TYPE	PLATE	1	108.30	60.30	27.92
2	PROVINCE	TYPE	PLATE	REG	1	117.20	60.00	36.82
3	PROVINCE	CRUST	PLATE	REG	1	128.76	62.00	48.37
4	CRUST	TYPE	REG	TOPO	1	152.03	58.00	71.65
5	OROGEN	CRUST	TYPE	TOPO	1	188.21	58.00	107.83
6	OROGEN	CRUST	TYPE	REG	1	192.28	57.00	111.90
7	TYPE	PLATE	REG	TOPO	1	204.46	59.20	124.08
8	CRUST	TYPE	PLATE	TOPO	1	213.56	62.00	133.18
9	CRUST	TYPE	PLATE	GLiM	1	223.09	61.00	142.71
10	TYPE	REG	GLiM	TOPO	1	225.26	61.00	144.88
11	TYPE	PLATE	REG	GLiM	1	230.12	60.00	149.74
12	PROVINCE	OROGEN	TYPE	TOPO	1	230.21	61.00	149.83
13	PROVINCE	CRUST	TYPE	TOPO	1	230.82	63.00	150.44
14	PROVINCE	OROGEN	TYPE	REG	1	234.29	60.90	153.91
15	PROVINCE	CRUST	REG	TOPO	1	234.83	62.00	154.45
16	OROGEN	TYPE	PLATE	REG	1	237.45	64.00	157.07
17	OROGEN	CRUST	TYPE	GLiM	1	237.82	61.00	157.44
18	PROVINCE	TYPE	REG	TOPO	1	238.10	62.00	157.72
19	OROGEN	TYPE	REG	TOPO	1	238.99	62.80	158.60
20	PROVINCE	OROGEN	TYPE	GLiM	1	241.16	63.00	160.78
21	CRUST	TYPE	GLiM	TOPO	1	241.20	62.40	160.82
22	PROVINCE	OROGEN	CRUST	TYPE	1	242.14	58.00	161.76
23	OROGEN	TYPE	PLATE	TOPO	1	250.37	64.00	169.99
24	OROGEN	CRUST	REG	TOPO	1	255.52	61.00	175.14
25	OROGEN	CRUST	PLATE	TOPO	1	257.27	65.00	176.89
26	CRUST	TYPE	REG	GLiM	1	258.17	62.00	177.79
27	OROGEN	TYPE	REG	GLiM	1	258.86	64.30	178.48
28	CRUST	PLATE	REG	TOPO	1	261.80	63.00	181.42
29	PROVINCE	OROGEN	CRUST	TOPO	1	263.67	61.94	183.29
30	PROVINCE	OROGEN	REG	TOPO	1	263.96	63.00	183.58
31	OROGEN	TYPE	GLiM	TOPO	1	265.00	64.00	184.61
32	OROGEN	PLATE	REG	TOPO	1	267.10	65.00	186.72
33	TYPE	PLATE	GLiM	TOPO	1	268.86	64.00	188.48
34	PROVINCE	CRUST	PLATE	TOPO	1	271.58	66.00	191.20
35	CRUST	PLATE	GLiM	TOPO	1	275.03	64.00	194.65
36	PROVINCE	OROGEN	REG	GLiM	1	275.76	64.60	195.38
37	OROGEN	PLATE	GLiM	TOPO	1	275.78	64.00	195.40
38	PLATE	REG	GLiM	TOPO	1	276.15	63.20	195.77
39	PROVINCE	TYPE	PLATE	TOPO	1	277.38	64.00	197.00
40	PROVINCE	OROGEN	GLiM	TOPO	1	279.76	65.00	199.38
41	PROVINCE	PLATE	REG	TOPO	1	281.47	64.00	201.08
42	PROVINCE	OROGEN	PLATE	TOPO	1	282.12	65.00	201.74
43	OROGEN	REG	GLiM	TOPO	1	284.64	65.00	204.26
44	OROGEN	PLATE	REG	GLiM	1	286.99	64.77	206.61
45	OROGEN	TYPE	PLATE	GLiM	1	287.13	65.00	206.75
46	PROVINCE	CRUST	GLiM	TOPO	1	295.87	65.30	215.49
47	PROVINCE	CRUST	TYPE	GLiM	1	296.55	64.80	216.17
48	PROVINCE	TYPE	GLiM	TOPO	1	297.13	65.60	216.75
49	OROGEN	CRUST	GLiM	TOPO	1	298.82	65.00	218.44

	label_1	label_2	label_3	label_4	flag	q_mean	q_median	Diff
50	PROVINCE	REG	GLiM	TOPO	1	302.37	66.00	221.99
51	CRUST	REG	GLiM	TOPO	1	303.65	66.00	223.26
52	PROVINCE	PLATE	GLiM	TOPO	1	304.33	65.30	223.95
53	CRUST	PLATE	REG	GLiM	1	305.44	65.00	225.06
54	OROGEN	CRUST	PLATE	GLiM	1	311.21	66.00	230.83
55	PROVINCE	OROGEN	CRUST	GLiM	1	314.64	65.10	234.26
56	PROVINCE	CRUST	REG	GLiM	1	314.87	66.20	234.49
57	OROGEN	CRUST	REG	GLiM	1	315.34	65.60	234.96
58	PROVINCE	TYPE	PLATE	GLiM	1	319.77	66.00	239.39
59	PROVINCE	OROGEN	CRUST	REG	1	344.40	60.60	264.02
60	PROVINCE	OROGEN	CRUST	PLATE	1	346.45	71.00	266.07
61	OROGEN	CRUST	PLATE	REG	1	364.79	69.00	284.40
62	PROVINCE	CRUST	TYPE	REG	1	373.22	67.00	292.84
63	OROGEN	CRUST	TYPE	PLATE	0	250.08	64.00	169.70
64	PROVINCE	OROGEN	TYPE	PLATE	0	295.89	67.00	215.50
65	PROVINCE	OROGEN	PLATE	GLiM	0	307.01	67.00	226.63
66	PROVINCE	CRUST	PLATE	GLiM	0	313.33	66.00	232.94
67	PROVINCE	TYPE	REG	GLiM	0	313.49	68.00	233.11
68	PROVINCE	PLATE	REG	GLiM	0	323.22	66.00	242.84
69	PROVINCE	OROGEN	PLATE	REG	0	331.32	69.00	250.94

Table S3. Iterative proportional fitting of all quadruple of auxiliary variables. Flag indicates converging matrix (1), or maximum iterations (N = 500) reached (0). We use the calculated weight to compute a weighted mean and a weighted median value. The table is sorted according to difference from estimated average global heat flow from Lucazeau (2019). Small difference is itself not an argument for the selected weighting variables, however large differences are not likely to improve estimates using the here presented weights. Mean of IHFC - global average (Lucazeau, 2019) is 124 $mW\,m^{-2}$. The mean of all calculated difference values is 114 $mW\,m^{-2}$

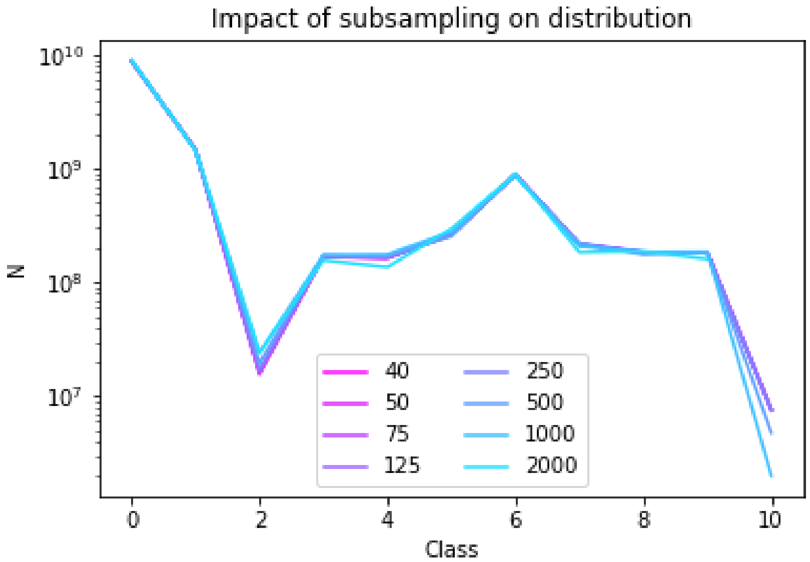

Figure S1. The relative distribution of classes from geomorphometrcs layer if sub-sampled N times. The y-axis shows the number of pixels for each class on a logarithmic scale

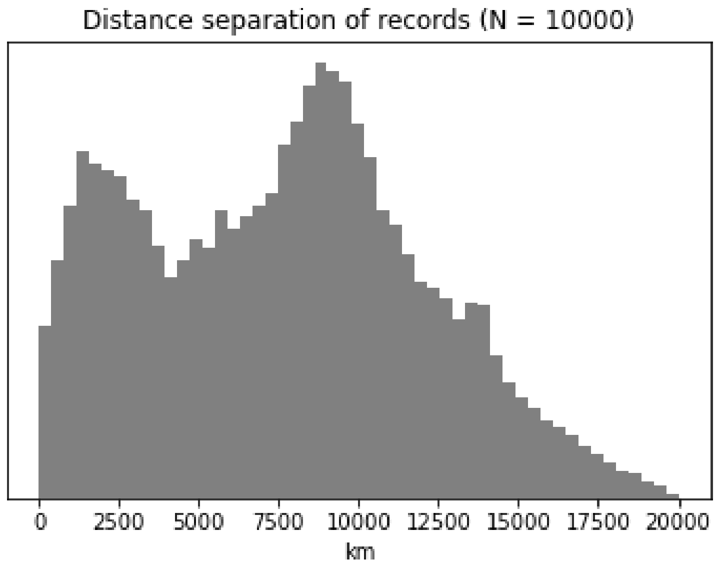

Figure S2. The distance between records (here as a sub-sample of N = 10 000) shows that most records are closely located and at the two main centre, North America and Europe, approximately 10 000 km apart.

5.2 Figures

The distribution of the geomorphometric layers are sub-sampled 40 times to limit the computational cost, however the impact on the distribution is marginal, as suggested in Figure S1

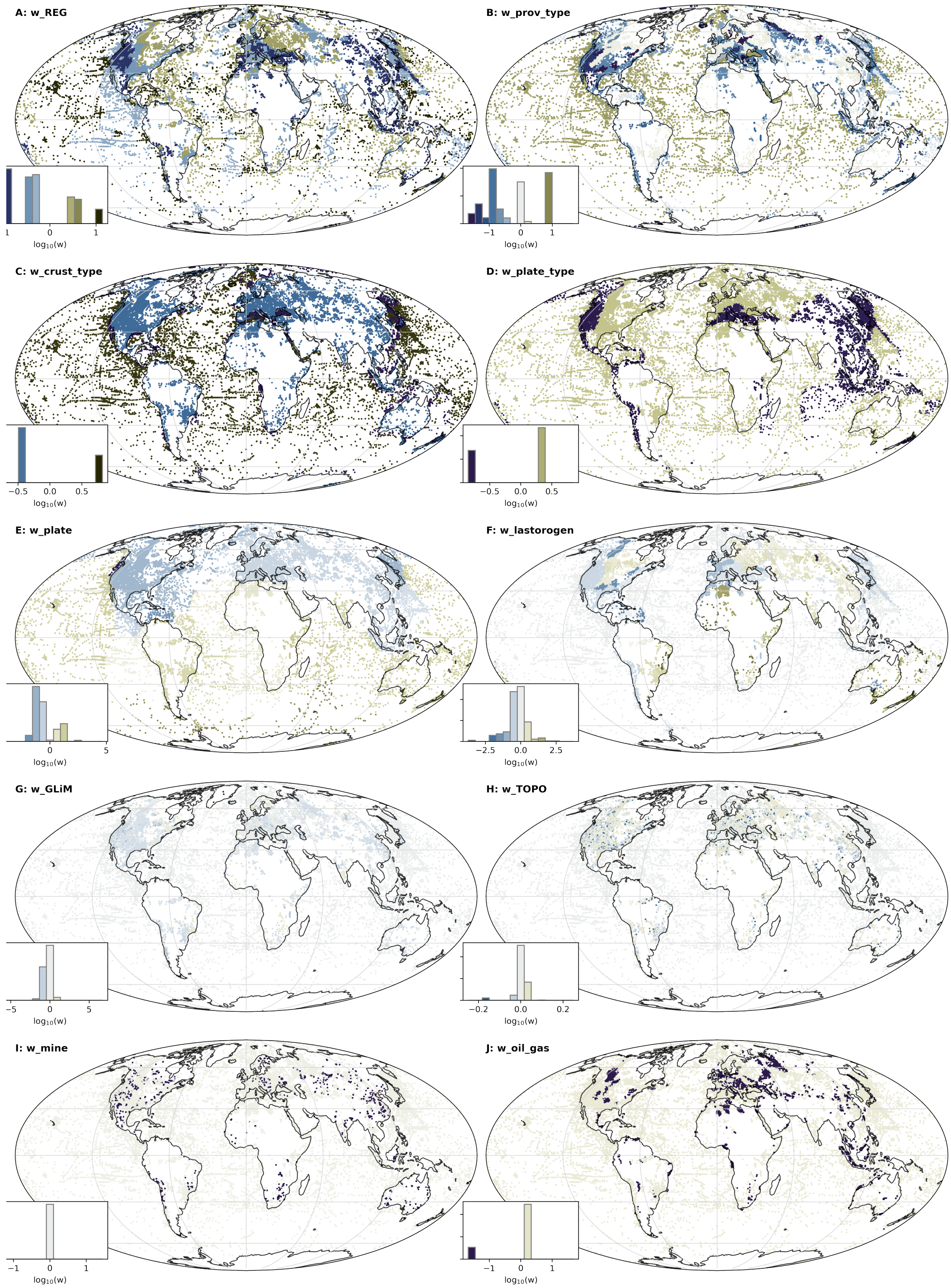

Figure S3. Maps of all ten weight distributions: **(A)** Weights calculated from (Schaeffer and Lebedev, 2015) **(B)** Weights calculated from Provenance (Hasterok et al., 2022). **(C)** Weights calculated from Crustal types (Hasterok et al., 2022). **(D)** Weights calculated from Tectonic plate types (Hasterok et al., 2022). **(E)** Weights calculated from Tectonic Plates (Hasterok et al., 2022). **(F)** Weights calculated from Latest orogens (Hasterok et al., 2022). **(G)** Weights calculated from Lithological classes (Hartmann and Moosdorf, 2012). **(H)** Weights calculated from Geomorphometric shapes (Amatulli et al., 2020). **(I)** Weights calculated from mining regions, **(J)** Weights calculated from oil and gas fields,

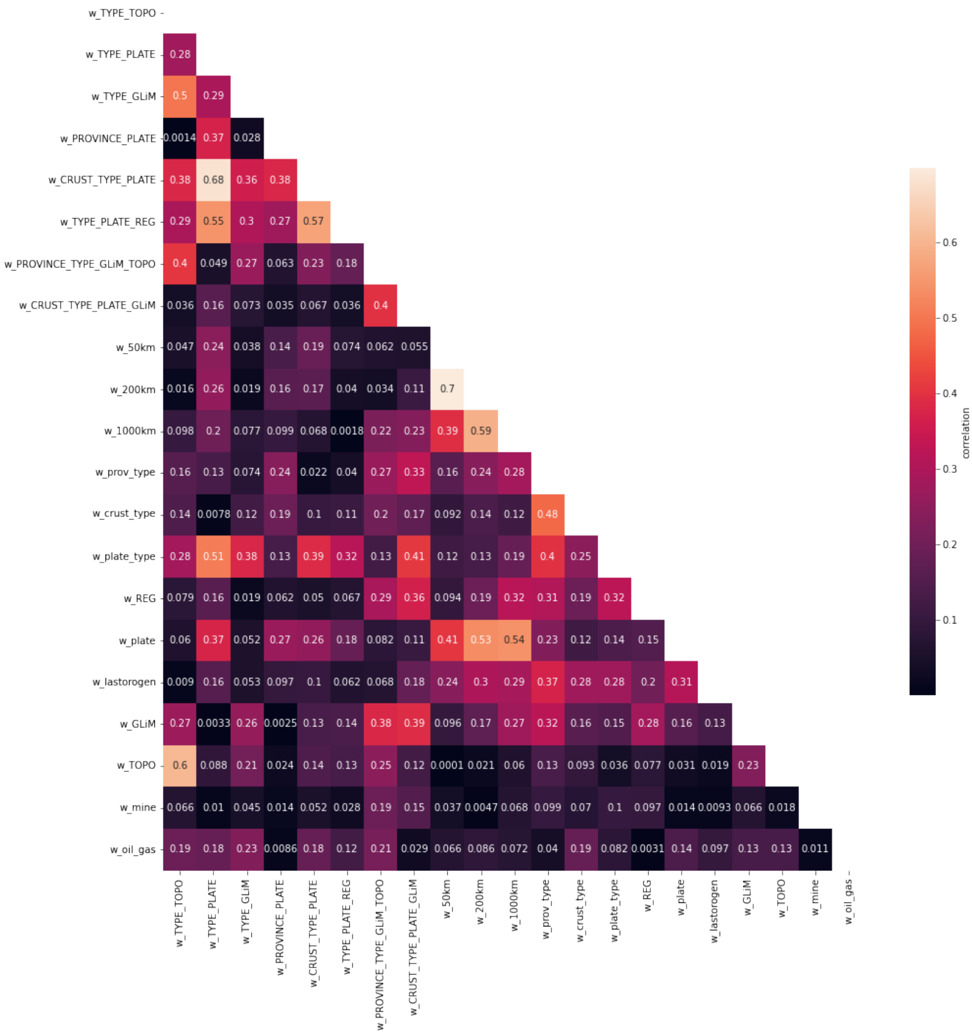

Figure S4. Correlation matrix of weights, showing Kendall rank correlation coefficient (Kendall τ). The weight correlations are considered when selecting variables for iterative proportional fitting. As expected, there is no strong non-trivial correlation of geology. The matrix was initially used to select weights ti fit, however here shown containing also the fitted weights and geometric weights

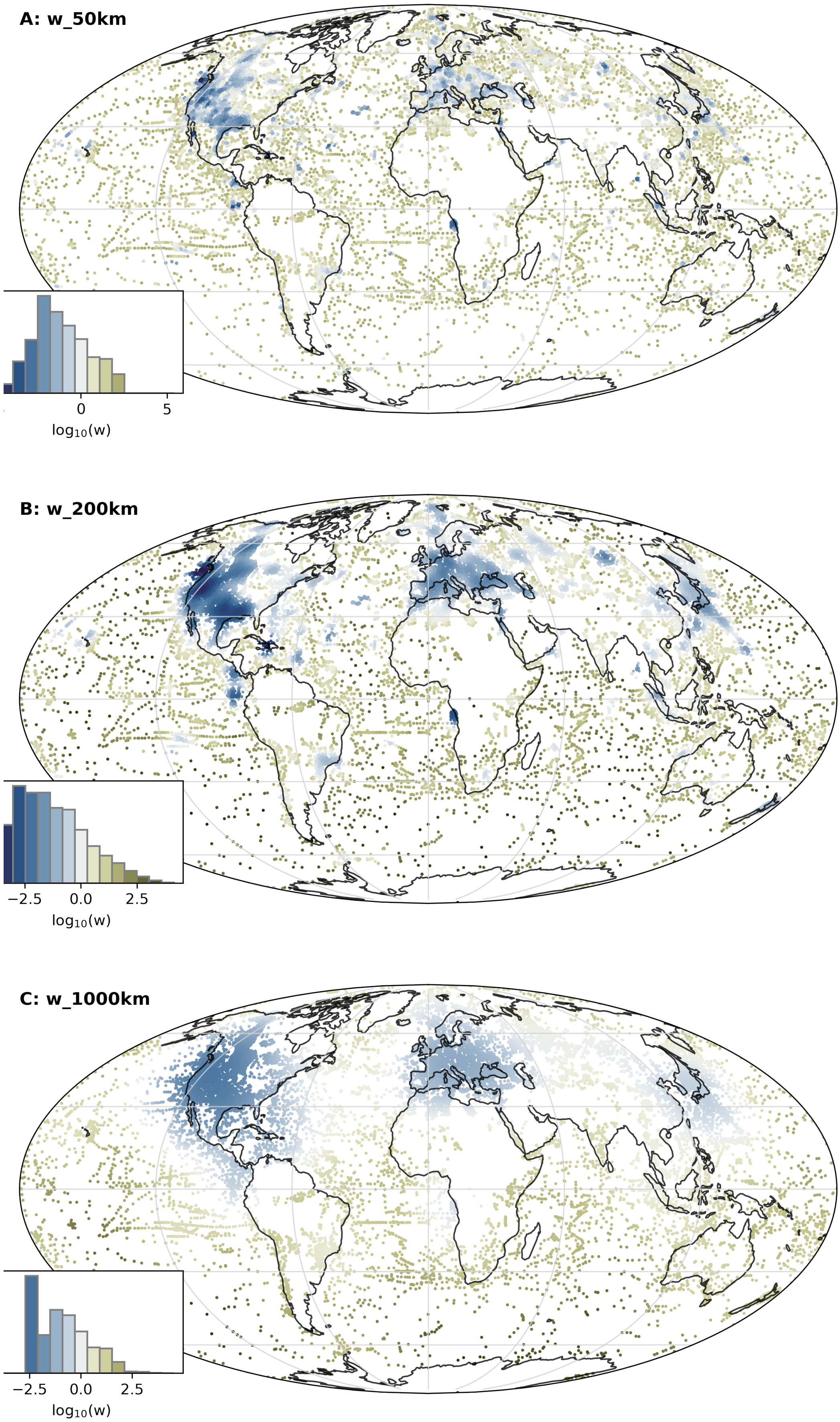

Figure S5. Distance weighting for three kernels. **(A)** σ = 50 km Gaussian kernel. **(B)** σ = 100 km Gaussian kernel, and **(C)** σ = 150 km Gaussian kernel